Enhancement of photocatalytic hydrogen evolution activity of g-C$_3$N$_4$ induced by structural distortion via post-fluorination treatment

Lei Zeng[a,b], Xue Ding[a], Zongzhao Sun[a], Weiming Hua[b], Wulin Song[c,d], Shuangyi Liu[a,e], Limin Huang[a,*]

[a] *Department of Chemistry, Southern University of Science and Technology of China, Shenzhen, PR China*
[b] *Department of Chemistry, Fudan University, Shanghai, PR China*
[c] *State Key Laboratory of Materials Processing and Die & Mould Technology, Huazhong University of Science and Technology, Wuhan, PR China*
[d] *Analysis and testing center, Huazhong University of Science and Technology, Wuhan, PR China*
[e] *Chongqing Institute of Green & Intelligent Technology, Chinese Academy of Sciences, Chongqing 400714, PR China*

ARTICLE INFO

ABSTRACT

Graphic carbon nitride (g-C$_3$N$_4$) has recently attracted a great deal of attention for its application in solar energy conversion. The photocatalytic activities, however, suffer from fast electron-hole recombination and insufficient solar absorption of g-C$_3$N$_4$. Here, a modified g-C$_3$N$_4$ (CNF) photocatalyst, which was prepared by a simple hydrothermal treatment with dilute hydrofluoric acid (0.1 M HF), has achieved a 2.4-fold enhanced photocatalytic activity for hydrogen production under visible light irradiation compared to pristine g-C$_3$N$_4$. It is demonstrated that a structural distortion is introduced in the CNF sheets without the formation of C−F bonds after the hydrothermal treatment, which can effectively separate photogenerated electron-hole pairs. Interestingly, the g-C$_3$N$_4$ treated by oil bath reflux reaction with dilute hydrofluoric acid (CNFO) under the same reaction condition (concentration, temperature and duration) has no sign of structural distortion, and shows a decline in the photocatalytic H$_2$ evolution activity. This may be attributed to the enhanced localization mobility of π electrons induced by the formation of C−F bonds after the oil bath treatment. These findings provide a better understanding on the effect of different fluorination treatments on the surface states and photocatalytic activities of g-C$_3$N$_4$-based materials. Additionally, this work presents a promising strategy to improve the photocatalytic H$_2$ evolution activity of g-C$_3$N$_4$ or related polymer semiconductors via microstructure engineering.

1. Introduction

As fossil energy reserves decrease ceaselessly, many efforts have been made to find new substitutes. Hydrogen is one of the ideal alternative candidates that can be used in fuel cells to generate electricity with water as an only product and no carbon emission. Moreover, hydrogen can be generated from water which is abundant on the earth. Therefore, the most challenging yet promising process for hydrogen evolution is water splitting by catalysis, including electrochemical catalysis and photocatalysis using solar energy [1–5]. It is believed that the exploitation and development of highly efficient photocatalysts for hydrogen production may solve the energy crisis and mitigate the global warming.

Graphitic carbon nitride (g-C$_3$N$_4$) has been widely used in water splitting for hydrogen generation, environmental remediation and energy storage [6–8] due to its excellent physicochemical property, including suitable band structure, chemical stability, cheap and easy

preparation since Wang et al. firstly introduced it to the photocatalytic field [9]. Especially, the appropriate conduction band position endows g-C$_3$N$_4$ excellent photocatalytic ability for hydrogen generation. However, low utilization of solar energy and severe recombination of electron-hole pairs still restrain the hydrogen production efficiency of g-C$_3$N$_4$. In recent years, a series of strategies have been developed to improve its photocatalytic activity, such as nanostructure design [10], exfoliation [11], elemental doping [12], copolymerization [13] and heterojunction construction [14]. Doping of heteroatoms has been regarded as an effective method to expand semiconductor's absorption range of solar spectrum since visible light active nitrogen-doped TiO$_2$ was developed by Asahi et al. [15]. For g-C$_3$N$_4$, nonmetal elements including boron [16–18], oxygen [19], fluorine [20], phosphorus [21], sulfur [22,23], bromine [24] and iodine [12] doped g-C$_3$N$_4$ have been successfully synthesized and exhibit significantly improved photocatalytic activity. Moreover, the enhancement of photocatalytic activity in the nonmetal element doped g-C$_3$N$_4$ is mainly ascribed to the red-

---

shift of absorption edge and up-shift of conduction band, but it is rarely reported that the enhancement arises from the acceleration of charge separation in the doped g-C_3N_4. Hence, it is necessary to find out an efficient approach to improve the charge separation for boosting photocatalytic activity of g-C_3N_4.

In the early research of g-C_3N_4, fluorine-containing inorganic salts were used as starting materials in the preparation of fluorine doped g-C_3N_4, and fluorine atom was used to expand the optical absorption range of g-C_3N_4 by replacing nitrogen atom [16,25]. It was found that fluorine dopant gave much less promotional effect on the optical absorption of g-C_3N_4 compared with other halogen dopants, even blue-shift of absorption edge occurred in fluorine modified g-C_3N_4. It was attributed to the high electronegativity of valence electrons in fluorine atoms, which can decrease the electron cloud density of π-electrons, and the mobility of electrons in π-system become more localized. Wang et al. [20] synthesized F-doped g-C_3N_4 with excellent photocatalytic activity by co-heating dicyanamide and NH_4F. Unfortunately, the transport property of charge carriers was not reported. Recently, it was reported that the charge separation can be improved in TiO_2 and g-C_3N_4 by microstructure engineering after fluorine doping. Yang et al. [26] successfully activated the inert rutile TiO_2 for high-performance photocatalytic hydrogen evolution by engineering a crystalline Ti^{3+} core/ amorphous Ti^{4+} structure after hydrogenation and fluorination. This smart design can regulate the transport behavior of electrons and holes from the bulk of a particle to the surface by suppressing the transport of electrons in conduction band and facilitating the transport of holes in valence band. Wang et al. [27] theoretically studied F-doped g-C_3N_4 as well as pristine g-C_3N_4 and proposed structural distortion to explain the reason for the enhanced photocatalytic activity of F-doped g-C_3N_4 for the first time. The structural distortion induced by fluorine doping and heat treatment significantly improves the photocatalytic activity of g-C_3N_4. The enhancement of photocatalytic activity can be attributed to the narrowed bandgap and the effective separation of photogenerated electron-hole pairs, which originate from the synergetic effect between fluorine doping and heat treatment. These results inspire us to consider which way of fluorination can improve the charge separation of g-C_3N_4 and the relationship between chemical state of fluorine atom and photocatalytic activity of g-C_3N_4.

In this paper, two kinds of modified g-C_3N_4 samples were synthesized by static hydrothermal reaction with dilute hydrofluoric acid (CNF) and by oil bath reflux reaction with the hydrofluoric acid (CNFO), respectively. To our surprise, C—F bonds only formed in CNFO sample, which showed a decline in photocatalytic activity for hydrogen evolution. However, CNF sample with no formation of C—F bonds exhibited an obvious improved photocatalytic activity. Characterization results demonstrated that a structural distortion is introduced in CNF sample and plays an important role in accelerating charge separation. On the other hand, the strong electronegativity of fluorine from C—F bonds enhances localized mobility of π-electrons in CNFO, which restrains the migration of charge carriers. These findings can deepen our understanding about the effect of electronegativity of doping atoms on the photocatalytic activity of g-C_3N_4 and provide a simple method that can effectively separate photogenerated electron-hole pairs via microstructure engineering.

2. Experimental section

2.1. Synthesis of photocatalysts

The typical synthesis of g-C_3N_4 involves the calcination of melamine as follows. In detail, 5 g of melamine was added to a crucible with a cover and calcined at 550 °C for 3 h at a heating rate of 5 °C/min in a muffle furnace, then the grinded powder was annealed at 500 °C for 2 h. The obtained sample (g-C_3N_4) was denoted as CN. For the post-fluorination, 0.15 g the obtained CN and 25 mL 0.1 M HF were added to a 50 mL Teflon lined autoclave and reacted at 160 °C for 10 h under static

condition, the obtained sample was washed with deionized water several times (denoted as CNF). For comparison, 0.15 g CN and 25 mL 0.1 M HF were added to a 50-mL flask to carry out oil bath reflux reaction at 160 °C for 10 h under ambient pressure, and the obtained sample was denoted as CNFO. In addition, 0.15 g CN and 25 mL deionized water were hydrothermally reacted at 160 °C for 10 h under static condition without HF, the obtained sample was denoted as CNH.

2.2. Characterization

X-ray diffraction (XRD) was conducted on a Rigaku smartlab system at 45 kV and 200 mA with Cu Kα radiation ($L_{K\alpha1} = 1.540593$ Å, $L_{K\alpha2} = 1.544414$ Å), at a scan rate of 5° min^{-1} and a step size of 0.020° in 2θ. Fourier transform infrared (FT-IR) measurements were recorded on KBr pellets using Bruker VERTEX 70 spectrophotometers. Transmission electron microscopy (TEM) was carried out on a FEI Tecnai F30 microscope at 300 kV. Atomic force microscopy (AFM) was performed using a Keysight Technologies (5500AFM/STM) scanning probe in tapping mode. The surface area analysis was performed from the nitrogen adsorption-desorption isotherms at 77 K with a Micromeritics Model ASAP 2020 instrument. The average pore diameter and pore volume of samples were calculated based on the Barrett−Joyner−Halenda (BJH) method. XPS with Al K X-rays radiation operated at 300 W (XPS: Kratos XSAM800 spectrometer, USA) was used to analyze the surface properties. The shift of binding energy due to relative surface charging was corrected using the C 1 s level at 284.8 eV as an internal standard. The spectra were fitted using a nonlinear least square fitting program (XPSPEAK) with a linear background and to the 80% Gaussian/20% Lorentzian peak shape. The EPR spectra were registered at room temperature in dark and under UV-light illumination respectively, using a Bruker EMXPlus-10/12-3.8k spectrometer at a microwave frequency of 9.8 GHz. The UV–vis absorbance spectra were obtained for the dry-pressed disk samples using a Scan UV–vis spectrophotometer (PerkinElmer, Lambda 950) equipped with an integrating sphere assembly. The spectra were recorded at room temperature in air within the range 200–800 nm. The steady-state photoluminescence spectra were gained by using a LabRAM HR spectrometer (HORIBA Jobin Yvon, France) with a laser excitation of 325 nm. The time-resolved spectroscopy was detected by a fluorescence spectrometer (F950) with an excitation wavelength of 365 nm and the signals were collected at excitation wavelength of 500 nm.

2.3. Electrochemical test

Electrochemical impedance spectroscopy (EIS), Mott-Schottky plot and transient photocurrent response were measured on electrochemical station (CHI660B, Shanghai Chenhua Limited, China) under ambient condition. All tests were performed on a conventional three-electrode cell in 0.5 M Na_2SO_4 solution. In detail, the carbon nitride electrode was prepared by dropping 10 μL aqueous slurry that consists of 5 mg of the prepared sample and 1 mL absolute ethanol containing 100 μL 0.05 wt % Nafion solution, on a glassy carbon electrode as the working electrode. A Pt wire and a standard Ag/AgCl electrode were used as the counter electrode and the reference electrode, respectively. The EIS was carried out in the frequency range of 0.01 Hz to 10^6 Hz with an AC voltage amplitude of 5 mV. Mott-Schottky tests were performed with the potentials ranging from 0 V to 1 V (vs. Ag/AgCl) at 1.7 kHz. The light source for transient photocurrent response measurement was a 10W LED lamp (wavelength range: 420–430 nm).

2.4. Photocatalytic hydrogen evolution test

The photocatalytic hydrogen evolution test was carried out in an online photocatalytic hydrogen production system (CEL-SPH2N, CEAULIGHT, Beijing). In detail, 50 mg of photocatalyst was added to an aqueous solution (40 mL 3 wt.% $H_2PtCl_6·6H_2O$ solution and 10 mL hole
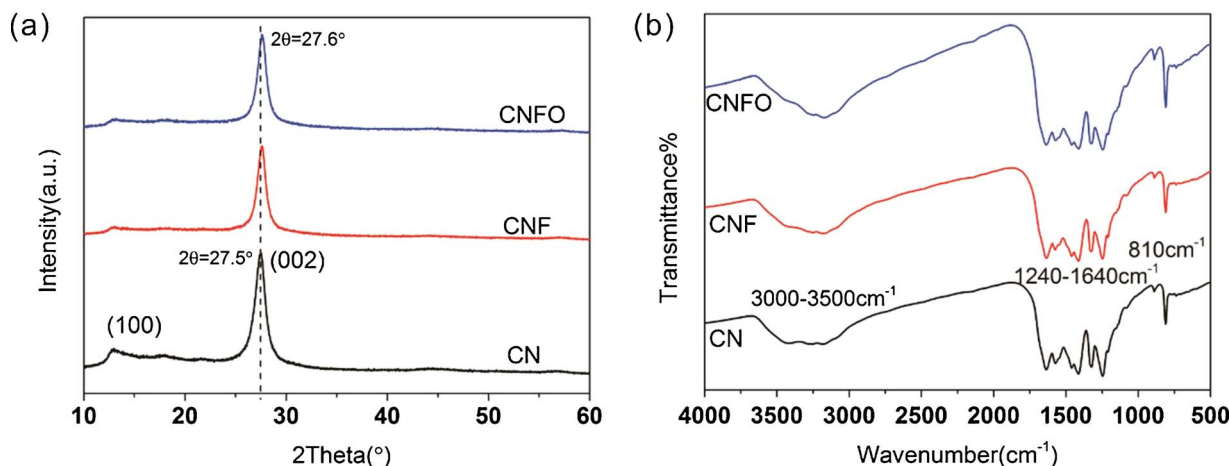
Fig. 1. (a) XRD patterns and (b) FTIR spectra for all samples.

sacrificial agent). Next, the solution was degassed and irradiated by a 300 W Xenon lamp (CEAULIGHT CEL-HXF300, Beijing) with a 420 nm filter. The photocatalytic H_2 evolution rate was determined by using an online gas chromatograph (GC D7860, TCD detector, N_2 carrier, 5A molecular sieve column, Shanghai Jinghe Chromatograph Co., Ltd). The apparent quantum yield (AQY) for H_2 evolution was measured using the 420 nm band-pass filter. The average intensity of irradiation was measured by a Coherent Fieldax-TO spectroradiometer. The AQY was estimated as

AQY (%) = 2*number of evolved H molecules/number of incident photons

3. Results and discussion

The X-ray diffraction patterns in Fig. 1a show a typical (002) interlayer-stacking peak at ~27.5° and the (100) peak at ~13° corresponding to in-plane ordering of tri-s-triazine units for all three samples. Both of the peaks, especially the (100) peak, become less intense after HF treatment, suggesting the disturbance of ordered graphitic structure by fluorination [20]. There are no observable shifts for the peaks at (100) and (002) after the treatment, suggesting that the hydrofluoric acid treatment cannot exfoliate g-C_3N_4 nanosheets under current conditions. The Fourier transform infrared spectra displayed in Fig. 1b also show a series of peaks belong to graphitic carbon nitride. A peak at 810 cm^{-1} is typical for out-of-plane bending mode of heptazine rings, while peaks located between 1240 and 1640 cm^{-1} originate from N−C=N hetero-rings in the melon framework [5,28]. The multiple broad peaks in 3000–3500 cm^{-1} correspond to N−H stretching vibrations. Both CNF and CNFO samples remain the tri-s-triazine based structure, indicating that the structure is not affected by the HF treatment. However, it is difficult to identify the stretching mode of C−F bonds (~1220 cm^{-1}) based on the IR result [20].

The TEM images in Fig. 2 show that CNF and CNFO samples maintain two-dimensional lamellar morphology after the treatment with dilute hydrofluoric acid (0.1 M HF). AFM characterization was carried out to find out the thickness variation, and the AFM images (Fig. S1) show that the thickness of CNF and CNFO is not much varied from that of CN. Hence, it is concluded that g-C_3N_4 is hard to be exfoliated by the HF treatment. In addition, the dilute HF shows more considerable erosion ability in oil bath reaction, causing some g-C_3N_4 nanosheets transform to small nanoparticles which adhere on the surface of CNFO, as shown in Figs. 2 and S2. Besides, the high resolution TEM images of CN samples display an amorphous structure due to the disordered atomic arrangement. However, the atomic arrangement of CNF is in a thoroughly distorted way (the orange dashed outline in Fig. 2D), and the distorted fringe lattices mainly locate in the thin edge of CNF (area

surrounded by orange dash line). In addition, no distorted fringe lattices can be found in CNFO sample (Fig. 2F). To confirm that the structural distortion only occurs under HF hydrothermal treatment, CNH sample was prepared under hydrothermal treatment without the addition of HF, and the TEM images of are shown in Fig. 2G and H. From the HRTEM image, although the similar disordered atomic arrangement to that in CN and CNFO is presented, no structural distortion can be found in CNH. It is confirmed that the structural distortion can only occur under HF hydrothermal treatment. In addition, the distorted fringe lattices still exist in CNF after five cycles of photocatalytic activity test, which shows the high stability in terms of microstructure (Fig. S2).

In Fig. 3a, it can be clearly seen that all samples exhibit type IV isotherms with H3 hysteresis loops in high relative pressure range between 0.5 and 1.0, suggesting that the obtained samples have mesoporous structures [29,30]. Based on the desorption curves, the BET surface area of CNF (53.2 m^2/g) and CNFO (20.3 m^2/g) is larger than that of CN (17.5 m^2/g), indicating that the hydrofluoric acid treatment can improve the surface area of g-C_3N_4, especially after the hydrothermal reaction. It may be related to the reduction in the size of nanosheets in CNF. In addition, CN and CNFO have a narrow pore size distribution which can be characterized by the presence of primarily a single type of pore with an average pore diameter of 37 nm. For CNF, apart from the pore diameter distribution centered at 35 nm, a few pores with diameters from 40 nm to 100 nm are also presented in Fig. 3b, which may be related to the increase of the surface area in CNF. Based on the characterization of microstructure, it is concluded that a structural distortion and increase of surface area can be induced by the hydrothermal reaction, while the structural distortion cannot occur in the oil bath reflux reaction.

The effect of hydrofluoric acid treatment on the electronic structure was also investigated. In Fig. 4a and b, it is clearly to see that a blueshift of UV–vis absorption edge has occurred after the treatment. Compared to CN with 2.7 eV bandgap, the bandgap increases to 2.74 eV for CNFO and 2.76 eV for CNF, which is consistent with the reports in literature [27]. In view of the steady PL spectra, an obvious blue shift of emission peak for CNF is exhibited in Fig. 4c. It also suggests that the bandgap of CNF has been widened, which is accordant with the results in UV—vis DRS spectra. In addition, the emission peaks located at 464 nm can be assigned to the electron transition from conduction bands to valence bands, and the intensity becomes the weakest in CNFO sample. It may be ascribed to the strong electronegativity of F atoms, which results in the enhanced localization of electrons in π system of g-C_3N_4. However, it cannot accurately reflect the recombination of photogenerated electrons and holes because it also relates to some surface states in semiconductors. To further investigate the mobility of
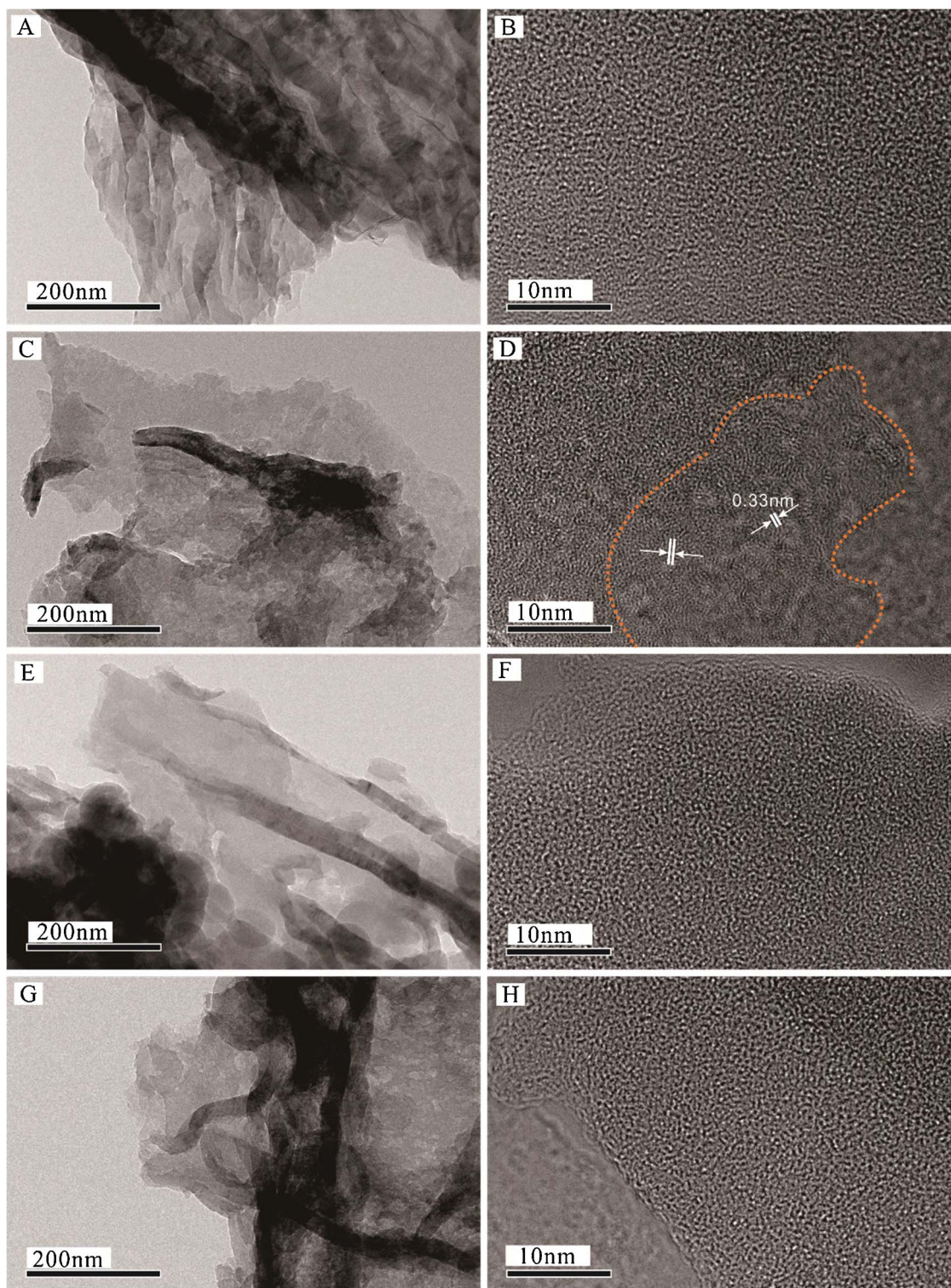
Fig. 2. TEM images and corresponding high resolution images for CN (A,B), CNF (C,D), CNFO (E,F) and CNH (G,H).

photogenerated charge carriers, the photoluminescence lifetime characterization has been carried out. The fitted lifetime of charge carriers is listed in Table S1. The results show that the fluorescence lifetime has a slight increase from 9.06 ns of CN to 13.55 ns of CNF while it decreases to 7.51 ns for CNFO. It indicates that the separation of photogenerated electron-hole pairs is enhanced in CNF with hydrothermal HF treatment, while it is weakened in CNFO with the oil bath reflux treatment. The improvement may be attributed to the existence of structural distortion at the edge of CNF. In addition, the acceleration on

the separation of photogenerated charge carriers was also verfied by Wang [27].

In order to explain the different effects of two hydrofluoric acid treatments on the photocatalytic activities between CNF and CNFO, the chemical states of F atoms in two samples were investigated by X-ray photoelectron spectroscopy (XPS). The C 1 s peaks of all samples can be fitted by two peaks, which are assigned to N−C═N (288.2 eV) and adventitious carbon species (284.8 eV) [31–33]. In addition, the N 1 s peaks of all samples can be deconvoluted into four peaks. The main
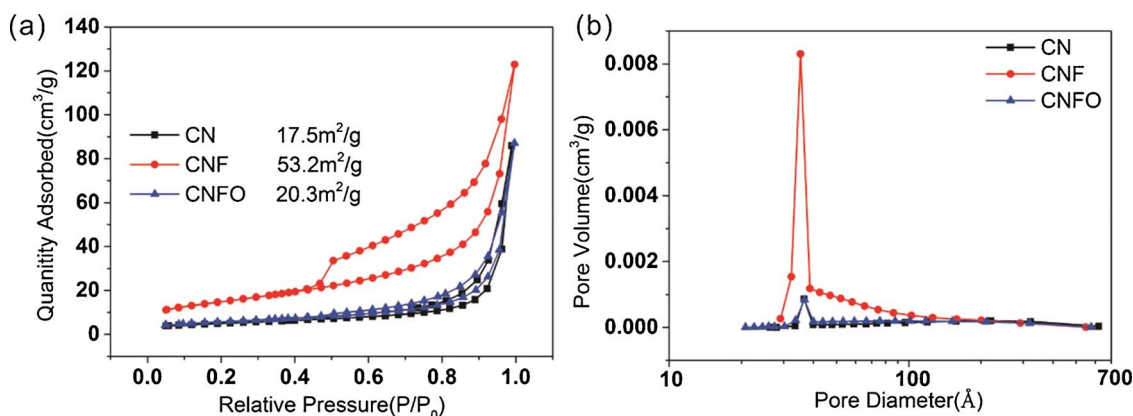
Fig. 3. N$_2$ isothermal adsorption-desorption curves (a) and pore-size distribution of CN, CNF and CNFO.

peak at 398.5 eV indicates the presence of sp^2-bonded N involved in the triazine rings (C−N═C). The peak at 399.8 eV is assigned to sp^3-bonded N (N-(C)$_3$). The peak located at 401.2 eV shows the occurrence of amino fuctional group (C−N−H), originating from the detective condensation of heptazine substructure. The weak peak at 404.4 eV maybe ascribed to the charging effect or positive charge localization in the heterocycles [11,34]. For F 1 s spectra, the signals only exist in CNF and CNFO samples with low intensity. The atomic concentrations of F are 0.31% and 0.25% in CNF and CNFO, respectively. However, the chemical states of fluorine in two samples are obviously distinct. The F 1 s peak can be deconvoluted into three peaks in CNFO, which correspond to surface physically adsorbed fluoride (684.8 eV) [35] and C−F bonds (686.2 eV) [16,20]. And, the peak located at 689.2 eV may be assigned to charge effect between fluorine atoms and π electorn system. The intensity of this peak in CNFO is stronger than that in CNF sample,

indicating that fluorine atoms show much stronger electron-with-drawing effect, which can be confirmed by EPR characterization. In the other side, the F 1 s spectrum in CNF sample can be deconvoluted into two peaks, located at 684.2 eV and 689.2 eV, respectively. No C−F bond is formed, indicating that g-C$_3$N$_4$ tends to be carbonized by hydro-thermal hydrofluoric acid treatment. It means that the passivation effect of hydrofluoric acid may play a major role during the hydrothermal reaction, which has been reported before [26]. Besides, to validate the exsitence of structural distortion in CNF, the intensity ratio of N-sp^2/N-sp^3 has been studied by XPS analysis, as shown in Fig. 5d. It is obviously seen that the intensity ratio of N-sp^2/N-sp^3 decreases in CNF, while it increases in CNFO. It indicate that some of N-sp^2 turns into N-sp^3 in CNF sample, suggesting that the C−N plane has been distorted. As we have known, more N-sp^3 means more structural distortion in the sample. On the other hand, the increase of N-sp^2/N-sp^3 in CNFO hints
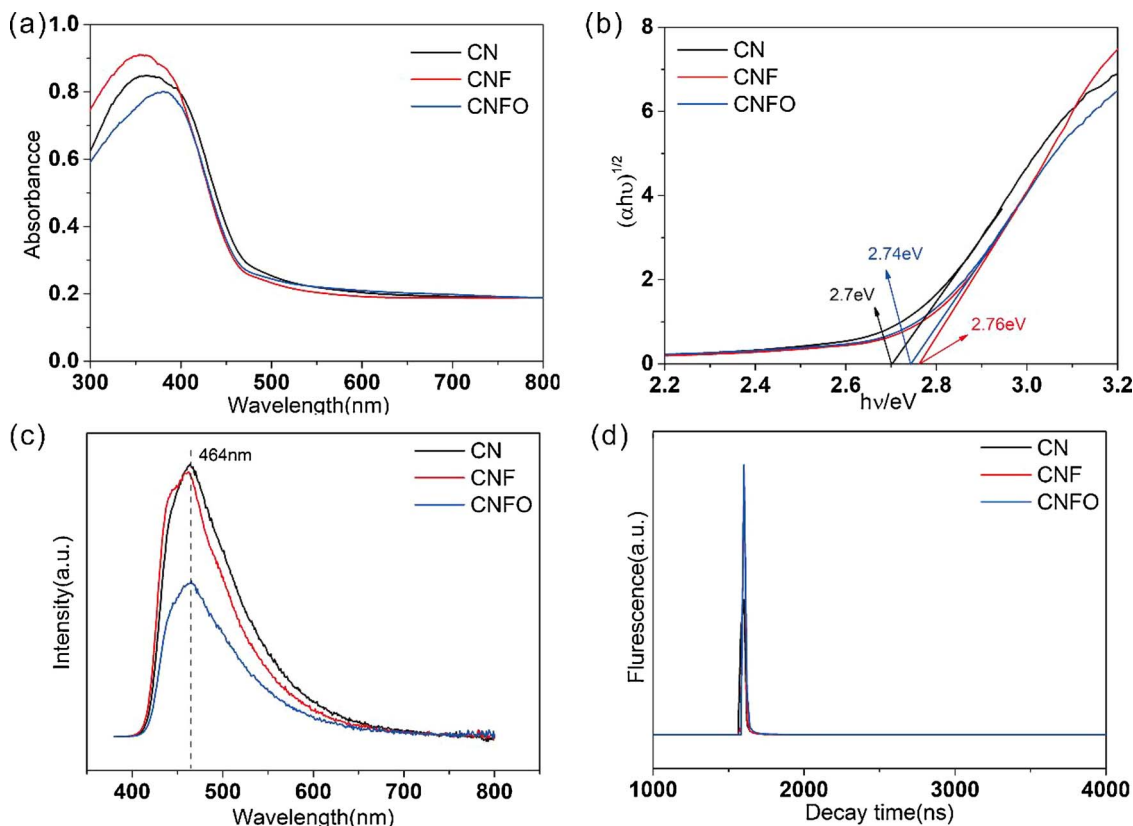

Fig. 4. (a) UV–vis absorption spectra and (b) the corresponding bandgaps of CN, CNF and CNFO. (c) Photoluminescence (PL) spectra and (d) the fitting curves of fluorescence decay of the samples.
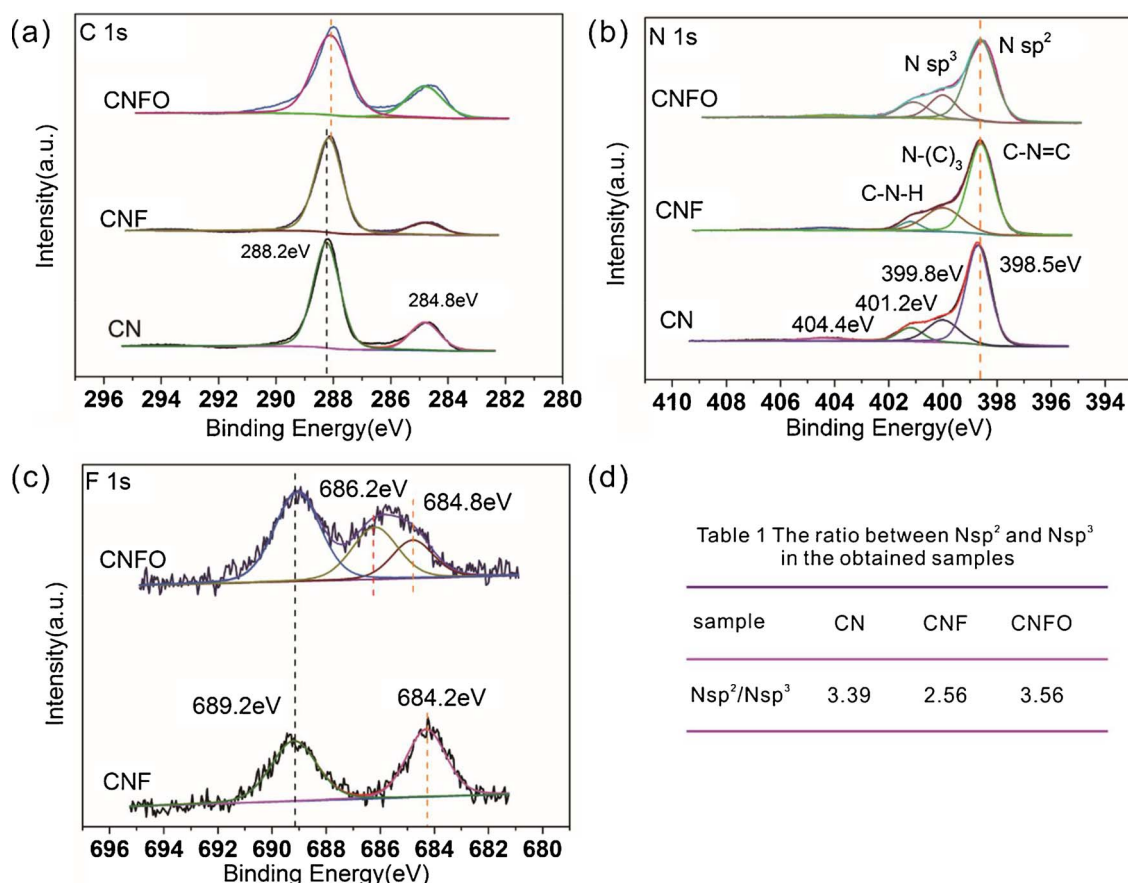
Fig. 5. High resolution XPS spectra of (a) C 1s, (b) N 1 s and (c) F 1 s for all samples. (d) The value of Nsp^2/Nsp^3 of the samples.

that the fluorine atoms successfully incorporate into the hepzine units and replace the nitrogen atoms, leading to the reduction of N-sp^3.

To further investigate the effect of fluorination on the microsturcture of g-C_3N_4, electron paramagnetic resonance (EPR) was used to find out whether the defects exist after the fluorination treatment. In Fig. 6a, both CN and CNF samples exhibit a single paramagnetic signal with the g value of 2.0034, which is attributed to unpaired electrons on sp^2-carbon atoms within the π-conjugated aromatic rings [36–38]. Moreover, no new paramagnetic signal appears in CNF sample and the signal with g value of 2.0034 is much enhanced compared with that in CN, indicating that the electrons in π system are more delocalized in CNF. However, there are three paramagnetic signals in CNFO, which may be ascribed to the energy level splitting induced by the incorporation of fluorine atoms into the C−N units. In addition, the paramagnetic signals in CN and CNF are both significantly enhanced after light illumination and the signal is more intensified in CNF, indicating that the delocalized mobility of electrons is enhanced after light illumination and charge separation is much improved in CNF. Surprisingly, the intensity of paramagnetic signal in CNFO after UV-light illumination is almost identical to that in dark, as shown in Fig. 6d. It demonstrates that the mobility of electrons in π system are intensively localized in CNFO. Compared with CNFO, the mobility of electrons in CNF is more delocalized. The transfer of charge carriers is affected significantly, which is reflected in the photocurrent of these samples, as shown in Fig. S3.

Fig. 7 shows the photocatalytic activities of CN, CNF, CNFO and CNH for hydrogen evolution under visible light illumination. As shown in Fig. 7a, the average hydrogen evolution rate of CNF is about 58.137 μmol/h (i.e. ~1167.7 μmol/h·g), which is 2.4 times higher than that of CN of 23.850 μmol/h (i.e. ~477.0 μmol/h·g), and 3.8 times higher than that of CNFO of 15.052 μmol/h (i.e. ~301.0 μmol/h·g),

respectively. The apparent quantum efficiency of CNF at 420 nm is 1.7%. In addition, it is clearly to see that the hydrogen evolution rate (25.547 μmol/h) of CNH is almost the same as that of CN, indicating that the dilute hydrofluoric acid plays a very important role in the formation of structural distortion and enhancement of photocatalytic activity. Furthermore, Fig. 7b clearly shows no significant decline in the photocatalytic activity for hydrogen evolution over CNF after five cycles of test, indicating the excellent photocatalytic stability of CNF sample.

Based on the above analysis, the distinct effects of different treatments with dilute hydrofluoric acid on the microstructure and band structure can be illustrated in Fig. 8. It is verified that a structural distortion has been introduced in CNF by hydrothermal treatment with dilute HF while it cannot be found in CNFO by oil bath reflux treatment. The structural distortion, which can significantly improve the separation of photogenerated electron-hole pairs in CNF, accounts for the remarkable increase in the photocatalytic activity for hydrogen evolution. It is attributed to that the distorted atomic arrangement of C−N planes can lead to delocalized electronic states in the bandgap, which prevents the fast recombination of charge carriers [12,27,39,40]. However, the separation of photogenerated charge carriers is inhibited by the formation of C−F bonds in CNFO due to enhanced localized mobility of π-electrons, which has been verified by EPR. The electrochemical impedance spectroscopy (EIS) is usually used to investigate the solid layer resistance and charge migration. The EIS Nyquist plots in Fig. S3b show that the radius of semicircle in CNF is the smallest, while that in CNFO is the largest. It suggests that the charge separation in CNF is more efficient. Besides, the VB-XPS spectra and Mott-Schottky measurement were also performed (Figs. S3c and S3d) to identify the band structure of samples. From Figs. S3c and S3d, it is clear to see that the negative shift of valence band (VB) and conduction band (CB) appears
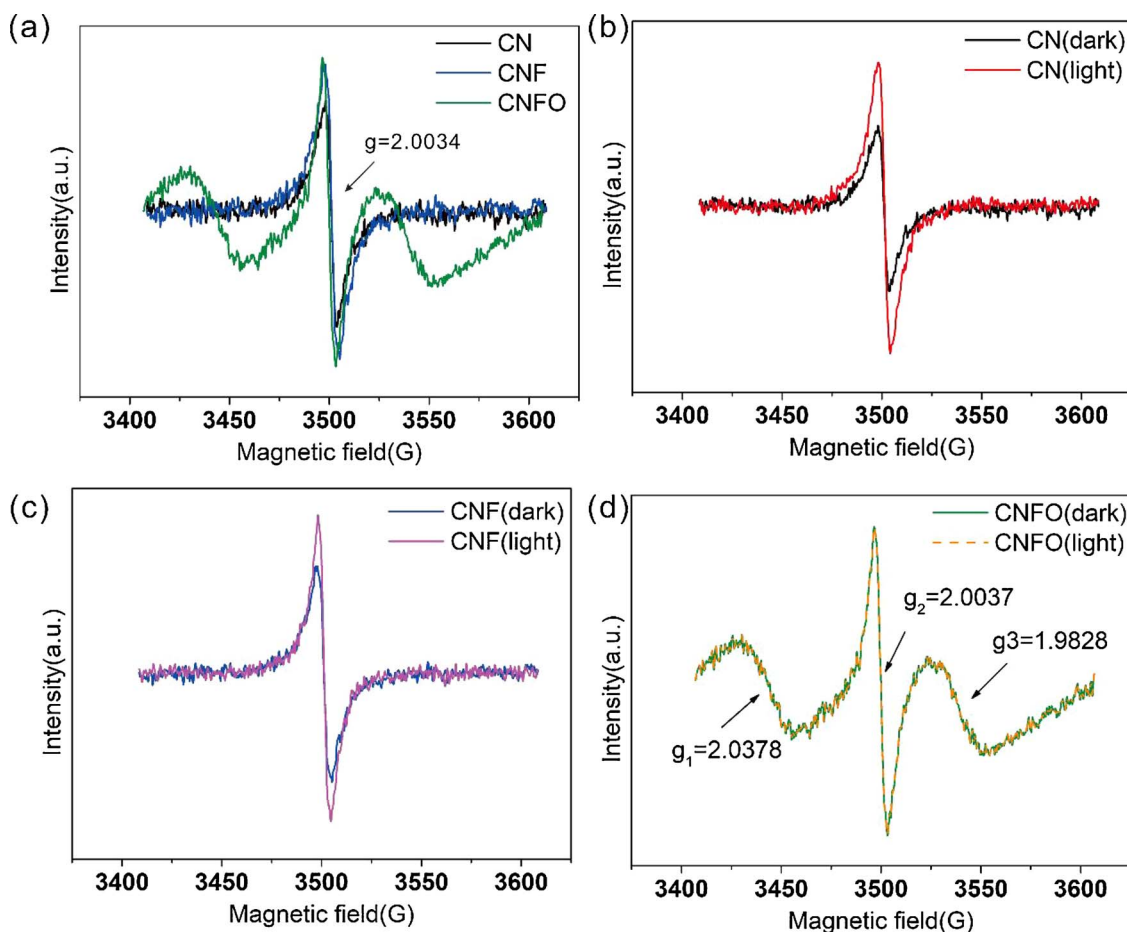
Fig. 6. EPR spectra for CN, CNF and CNFO measured at room temperature in dark (a), EPR spectra for CN (b), CNF (c) and CNFO (d) measured at room temperature in dark and under UV light illumination.

in CNF compared to that in CN while the positive-shift of VB and CB is evident in CNFO. Combined with the UV–vis diffuse reflectance spectra (DRS), the band structure of each sample can be described. In terms of thermodynamics, the more negative the CB potential is, the stronger the reductive ability of photogenerated electrons in CB is. In Fig. 8, the CB potential in CNF is obviously more negative than that in CN while it is more positive in CNFO. From a dynamic point of view, the charge separation in CNF is significantly improved compared with that in CN and CNFO by the introduction of structural distortion, which is also confirmed by electrochemical test and other characterization mentioned above. However, the enhanced localization of π-system electrons caused by the formation of surface C−F bonds leads to the fast

recombination of photogenerated electron-hole pairs in CNFO. Thus, the improved charge separation and negative-shift of CB in CNF is responsible for the enhancement of photocatalytic hydrogen production while the decline of photocatalytic activity for hydrogen evolution in CNFO is ascribed to the enhanced localization of electrons and the positive shift of CB.

4. Conclusion

In summary, two kinds of modified g-C_3N_4 were prepared by dilute hydrofluoric hydrothermal treatment (CNF) and oil bath refluxing treatment (CNFO), respectively. The CNFO sample with C−F bonds
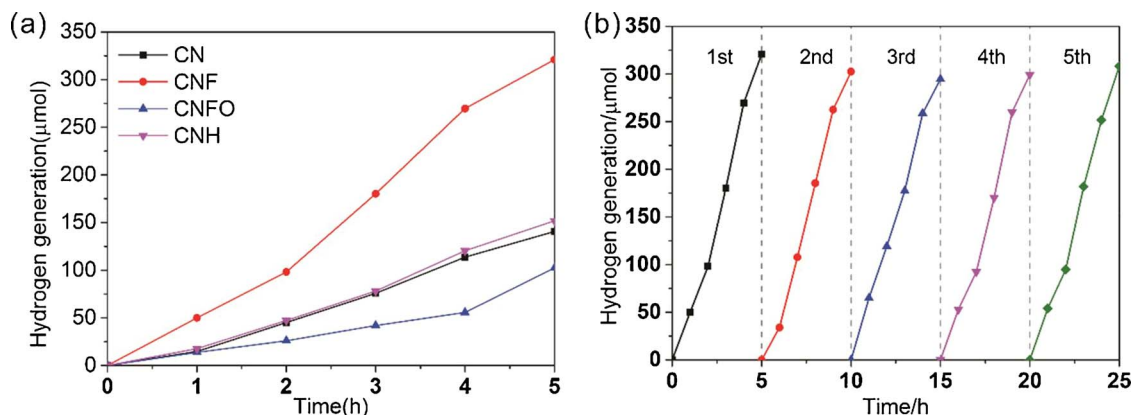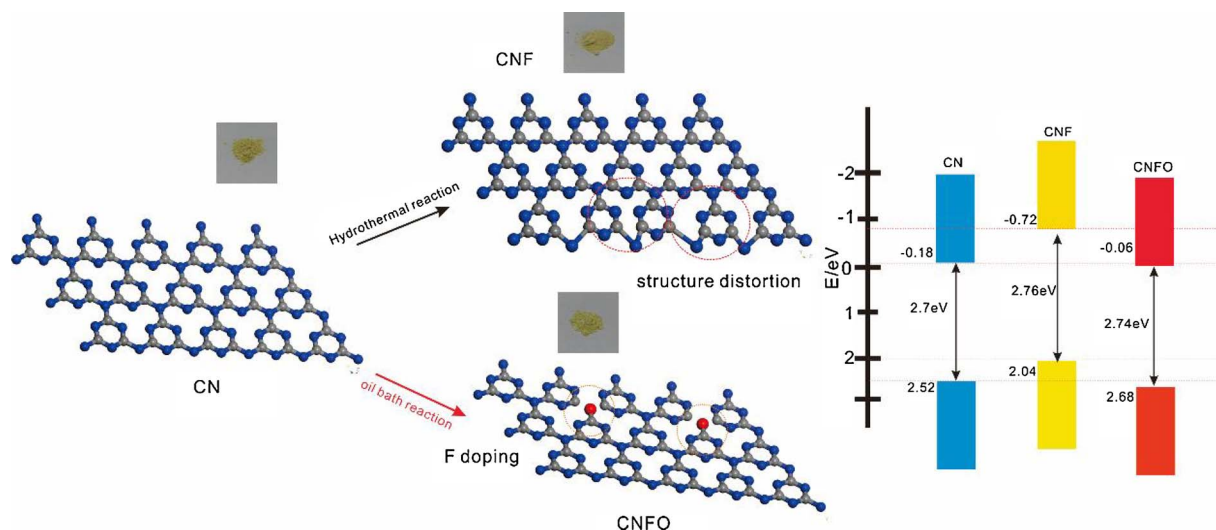

Fig. 7. (a) Photocatalytic activities for hydrogen generation over CN, CNF, CNFO and CNH. (b) Cycling measurements of hydrogen evolution for CNF.

Fig. 8. Illustration of the microstructure of g-C$_3$N$_4$ varied with different treatments with dilute hydrofluoric acid and proposed band structures. The microstructure is exaggerated to show the structural distortion and no other forms of fluorine modification but C−F bonds are presented for simplicity (C, N and F atoms are denoted with grey, blue and red balls, respectively. H atoms are neglected). (For interpretation of the references to colour in this figure legend, the reader is referred to the web version of this article.)

showed a decline in photocatalytic activity while CNF sample with structural distortion exhibited an obvious enhancement of photocatalytic activity. The structural distortion introduced by the HF hydrothermal treatment could significantly improve the charge separation in CNF. However, the mobility of unpaired electrons in π-system became more localized due to the formation of C−F bonds after the refluxing treatment, which restrained the migration of charge carriers in CNFO. In addition, it shows significant difference in band structure between CNF and CNFO. Compared to CN, the CB and VB in CNF show a negative-shift while the positive-shift appears in CNFO. Besides, the surface area was also increased in CNF sample due to the wider distribution of pore size. Thus, the photocatalytic activity for hydrogen evolution over CNF exhibited 2.4 times and 3.8 times higher than that over CN and CNFO, respectively. Our results provided an in-depth understanding on the relationship among fluorine modification, surface state and photocatalytic activity and pointed out a different path to engineering highly efficient g-C$_3$N$_4$ based photocatalysts with structural distortion.

Acknowledgements

Appendix A. Supplementary data

Supplementary data associated with this article can be found, in the online version, at https://doi.org/10.1016/j.apcatb.2018.01.040.

References

[1] H. Yu, R. Shi, Y. Zhao, T. Bian, Y. Zhao, C. Zhou, G.I.N. Waterhouse, L.Z. Wu, C.H. Tung, T. Zhang, Adv. Mater. 29 (2017) 16.
[2] X. Wu, F. Chen, X. Wang, H. Yu, Appl. Surf. Sci. 427 (2018) 645–653.
[3] X. Yang, Z. Chen, J. Xu, H. Tang, K. Chen, Y. Jiang, ACS Appl. Mater. Interfaces 7 (28) (2015) 15285–15293.
[4] W. Fu, H. He, Z. Zhang, C. Wu, X. Wang, H. Wang, Q. Zeng, L. Sun, X. Wang, J. Zhou, Q. Fu, P. Yu, Z. Shen, C. Jin, B.I. Yakobson, Z. Liu, Nano Energy 27 (2016) 44–50.
[5] Y. Zhao, F. Zhao, X. Wang, C. Xu, Z. Zhang, G. Shi, L. Qu, Angew. Chem. Int. Ed. Engl. 53 (50) (2014) 13934–13939.
[6] Juan Liu, Y.L., Naiyun Liu, Yuzhi Han, Xing Zhang, Hui Huang, Yeshayahu Lifshitz,* Shuit-Tong Lee,* Jun Zhong, Zhenhui Kang*, Science, 2015, 347(6225), 970.
[7] Q. Pang, L.F. Nazar, ACS Nano 10 (4) (2016) 4111–4118.
[8] S. Ma, S. Zhan, Y. Jia, Q. Shi, Q. Zhou, Appl. Catal. B: Environ. 186 (2016) 77–87.
[9] X. Wang, K. Maeda, A. Thomas, K. Takanabe, G. Xin, J.M. Carlsson, K. Domen, M. Antonietti, Nat. Mater. 8 (1) (2009) 76–80.
[10] D. Zheng, C. Huang, X. Wang, Nanoscale 7 (2) (2015) 465–470.
[11] Q. Han, B. Wang, J. Gao, Z. Cheng, Y. Zhao, Z. Zhang, L. Qu, ACS Nano 10 (2) (2016) 2745–2751.
[12] G. Zhang, M. Zhang, X. Ye, X. Qiu, S. Lin, X. Wang, Adv. Mater. 26 (5) (2014) 805–809.
[13] X. Fan, L. Zhang, R. Cheng, M. Wang, M. Li, Y. Zhou, J. Shi, ACS Catal. 5 (9) (2015) 5008–5015.
[14] G. Gao, Y. Jiao, E.R. Waclawik, A. Du, J. Am. Chem. Soc. 138 (19) (2016) 6292–6297.
[15] R. Asahi, T. Morikawa, T. Ohwaki, K. Aoki, Y. Taga, Science 293 (5528) (2001) 269–271.
[16] Y. Wang, J. Zhang, X. Wang, M. Antonietti, H. Li, Angew. Chem. Int. Ed. Engl. 49 (19) (2010) 3356–3359.
[17] K. Ding, L. Wen, M. Huang, Y. Zhang, Y. Lu, Z. Chen, Phys. Chem. Chem. Phys. 18 (28) (2016) 19217–19226.
[18] S.C. Yan, Z.S. Li, Z.S. Zou, Langmuir 26 (6) (2010) 3894–3901.
[19] J. Li, B. Shen, Z. Hong, B. Lin, B. Gao, Y. Chen, Chem. Commun. (Camb.) 48 (98) (2012) 12017–12019.
[20] Y. Wang, Y. Di, M. Antonietti, H. Li, X. Chen, X. Wang, Chem. Mater. 22 (18) (2010) 5119–5121.
[21] J. Ran, T.Y. Ma, G. Gao, X.-W. Du, S.Z. Qiao, Energy Environ. Sci. 8 (12) (2015) 3708–3717.
[22] J. Zhang, J. Sun, K. Maeda, K. Domen, P. Liu, M. Antonietti, X. Fu, X. Wang, Energy Environ. Sci. 4 (3) (2011) 675–678.
[23] C. Xu, Q. Han, Y. Zhao, L. Wang, Y. Li, L. Qu, J. Mater. Chem. A 3 (5) (2015) 1841–1846.
[24] Z.-A. Lan, G. Zhang, X. Wang, Appl. Catal. B: Environ. 192 (2016) 116–125.
[25] D. Gao, Y. Liu, M. Song, S. Shi, M. Si, D. Xue, J. Mater. Chem. C 3 (47) (2015) 12230–12235.
[26] Y. Yang, G. Liu, J.T. Irvine, H.M. Cheng, Adv. Mater. 28 (28) (2016) 5850–5856.
[27] H. Wang, X. Zhang, J. Xie, J. Zhang, P. Ma, B. Pan, Y. Xie, Nanoscale 7 (12) (2015) 5152–5156.
[28] Y. Cui, G. Zhang, Z. Lin, X. Wang, Appl. Catal. B: Environ. 181 (2016) 413–419.
[29] S. Guo, Y. Zhu, Y. Yan, Y. Min, J. Fan, Q. Xu, Appl. Catal. B: Environ. 185 (2016) 315–321.
[30] L. Lin, H. Ou, Y. Zhang, X. Wang, ACS Catal. 6 (6) (2016) 3921–3931.
[31] J. Liu, S. Xie, Z. Geng, K. Huang, L. Fan, W. Zhou, L. Qiu, D. Gao, L. Ji, L. Duan, L. Lu, W. Li, S. Bai, Z. Liu, W. Chen, S. Feng, Y. Zhang, Nano Lett. 16 (10) (2016) 6568–6575.
[32] L. Sun, M. Yang, J. Huang, D. Yu, W. Hong, X. Chen, Adv. Funct. Mater. 26 (27) (2016) 4943–4950.
[33] Q. Han, B. Wang, J. Gao, L. Qu, Angew. Chem. Int. Ed. Engl. 55 (36) (2016) 10849–10853.

[34] Y. Zhang, Z. Zhou, Y. Shen, Q. Zhou, J. Wang, A. Liu, S. Liu, Y. Zhang, ACS Nano 10 (9) (2016) 9036–9043.

[35] C. Jimmy, J.Y. Yu, Wingkei Ho, Zitao Jiang, Lizhi Zhang, Chem. Mater. 14 (2002) 3808–3816.

[36] G. Liu, G. Zhao, W. Zhou, Y. Liu, H. Pang, H. Zhang, D. Hao, X. Meng, P. Li, T. Kako, J. Ye, Adv. Funct. Mater. 26 (37) (2016) 6822–6829.

[37] Z. Hong, B. Shen, Y. Chen, B. Lin, B. Gao, J. Mater. Chem. A 1 (38) (2013) 11754.

[38] J. Zhang, X. An, N. Lin, W. Wu, L. Wang, Z. Li, R. Wang, Y. Wang, J. Liu, M. Wu, Carbon 100 (2016) 450–455.

[39] X. Chen, L. Liu, P.Y. Yu, S.S. Mao, Science 331 (6018) (2011) 746–750.

[40] Y. Zhang, M. Antonietti, Chem. Asian J. 5 (6) (2010) 1307–1311.